# A Dynamic Model for Six-Degree-of-Freedom Bearingless Linear Motor Systems

Reza Hosseinzadeh, Floran Martin, and Marko Hinkkanen, *Senior Member, IEEE*

***Abstract*—This article develops a dynamic model for six-degree-of-freedom bearingless linear motor systems by means of lumped-element modeling. A four-sided motor system, containing eight three-phase motor units fed by their own inverters, is considered as an example system, but the modeling approach can be applied to other motor systems as well. The mechanical subsystem of the model comprises the rigid-body dynamics. The electromagnetic subsystem governs the electrical dynamics of the motor units and the production of the resultant electromagnetic force and its associated torque. In order to model the unbalanced magnetic torque due to tilting of the mover, the motor units are spatially discretized into a number of identical submotor models having a uniform air gap. The submotor models of each motor unit are electrically connected in series, i.e., they share the same current, but their flux linkages and forces differ in tilted positions. The electromagnetic subsystem can be parameterized based on simple static two-dimensional finite-element method computations at a range of uniform air-gap and current values. The developed model is validated through a comparison between the time-domain simulation results and the experimental results. The model can be applied to time-domain simulations, real-time control system development, and various analyses of the system.**

***Index Terms*—Bearingless, electromagnetic, linear actuator, lumped element, magnetic levitation, unbalanced magnetic pull.**

## I. Introduction

DIRECT-DRIVEN linear motors could efficiently replace rotating motors and rotary-to-linear conversion mechanisms in many transportation systems [1], [2], such as ropeless elevators [3]–[12]. In this kind of systems, a short mover travels along a long stationary rail. In order to reduce the costs, the long rail should exclude permanent magnets, windings, power electronics, and other expensive components. From this perspective, a linear flux-switching permanent-magnet (FSPM) motor, shown in Fig. 1, is of interest, as explained in [10]–[12]. In this motor type, the permanent magnets and the windings are placed to the short mover, while the long rail is only made of iron [13]–[19]. The linear FSPM motor exhibits sinusoidal back electromotive force (EMF), and it can be modeled and controlled based on a direct-quadrature ($dq$)-axis model. Thrust densities similar to those of conventional permanent-magnet motors have been reported [1], [20].

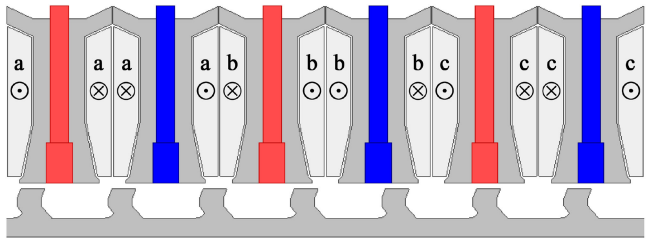


Fig. 1. Prototype three-phase linear FSPM motor unit. The positive direction of the coil currents are shown by crosses and dots.

Magnetic levitation systems have many advantages, such as contact-free and lubrication-free operation, no mechanical wear, long lifetime, and low vibration [21]. Recently, magnetically levitated linear actuators have been suggested for transportation systems and ropeless elevators [3]–[5], [12], [22]–[24], pick-and-place robots [25], [26], and providing linear oscillatory motion [27]. In these systems, either active magnetic bearings [4], [5], [25], [28] or bearingless motors [3], [12], [22]–[27] could be used. In bearingless linear systems, thrust-force-producing motor units also stabilize some [3], [23], [26] or all [12] the remaining mechanical degrees of freedom. If mechanical bearings and their supporting structures are avoided, the mover becomes lighter. This weight reduction is beneficial in battery-powered systems, where the batteries are located in the mover. A lower mover weight reduces the required thrust force and the battery pack size. Battery charging and required communication could be implemented using existing wireless technologies [29].

The focus of this article is on the development of a dynamic model for six-degree-of-freedom (6DOF) bearingless linear motor systems. A four-sided bearingless linear motor system [12], containing eight three-phase FSPM motor units fed by their own inverters, is considered as an example system. Nevertheless, the modeling approach is more general and can be applied to other motor types and geometrical configurations. Fig. 2 shows schematic cross-section views of this 6DOF mechanical system. Motor units are composed of an armature attached to the mover and a salient magnetic circuit fixed to the static rail.

Fig. 1 shows the geometry of the prototype linear FSPM motor units. All eight motor units contribute to the thrust force.

Manuscript received December 10, 2020; revised March 4, 2021; accepted April 23, 2021. Date of publication May 4, 2021; date of current version November 19, 2021. This work was supported in part by the KONE Corporation. Paper 2020-MLMS-1586.R1 approved for publication in the IEEE Transaction on Industry Applications by the Magnetically Levitated Motor Systems of the IEEE Industry Applications Society. *(Corresponding author: Reza Hosseinzadeh.)*

The authors are with the Department of Electrical Engineering and Automation, School of Electrical Engineering, Aalto University, 02150 Espoo, Finland (e-mail: reza.hosseinzadeh@aalto.fi; floran.martin@aalto.fi; marko.hinkkanen@aalto.fi).

Color versions of one or more figures in this article are available at https://doi.org/10.1109/TIA.2021.3077354.

Digital Object Identifier 10.1109/TIA.2021.3077354

This work is licensed under a Creative Commons Attribution 4.0 License. For more information, see https://creativecommons.org/licenses/by/4.0/

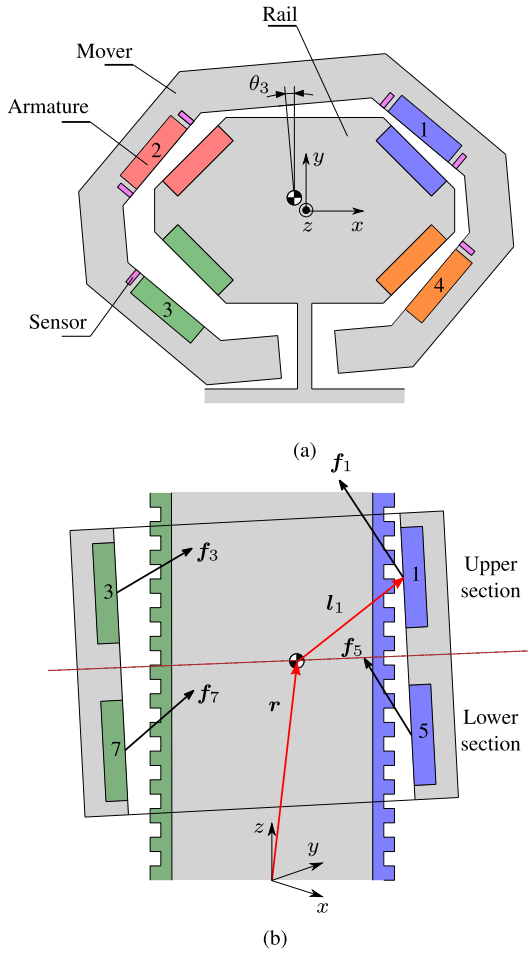


Fig. 2. Schematic cross-sectional views of a bearingless linear motor system. (a) Top view: Upper section motor units. (b) Side view: The mass-center position and orientation of the mover are defined by the vectors $\boldsymbol{r} = [x, y, z]^{\mathrm{T}}$ and $\boldsymbol{\theta} = [\theta_1, \theta_2, \theta_3]^{\mathrm{T}}$, respectively. The system contains eight motor units and 12 air-gap sensors. The force vectors $\boldsymbol{f}_i$ $(i = 1 \ldots 8)$ produced by the motor units are shown. The lever arm vector $\boldsymbol{l}_1$ related to motor unit 1 is also shown.

Furthermore, since the motor units are positioned in an opposing four-sided configuration, the magnetic levitation of the mover can be realized by properly controlling their normal attractive forces [23]. However, the control of this open-loop unstable system is challenging due to the nonlinear interaction between the electromagnetic and mechanical subsystems, manifesting itself as unbalanced magnetic forces and associated unbalanced torques. Both translational and rotational motions of the mover must be managed, the rotation around the $z$-axis (cf. Fig. 2) being the most challenging direction. A dynamic model of the open-loop system is required for analysis purposes, time-domain simulations, and real-time control development.

The main contribution of this article is to develop a dynamic lumped-element model for the 6DOF bearingless linear motor, including the nonlinear interaction between the mechanics and the electromagnetics. The mechanical subsystem of the model comprises the 6DOF rigid-body dynamics. The electromagnetic subsystem governs the electrical dynamics of the motor units and the production of the resultant electromagnetic force and its associated torque. To account for the unbalanced magnetic torque due to tilting of the mover, the motor units are spatially discretized into a number of identical submotor models, each having a uniform air gap. The submotor models of each motor unit are electrically connected in series, i.e., they share the same current, but their flux linkages and forces differ in tilted positions. The submotor model corresponds to a recent 2DOF bearingless linear motor model [24].

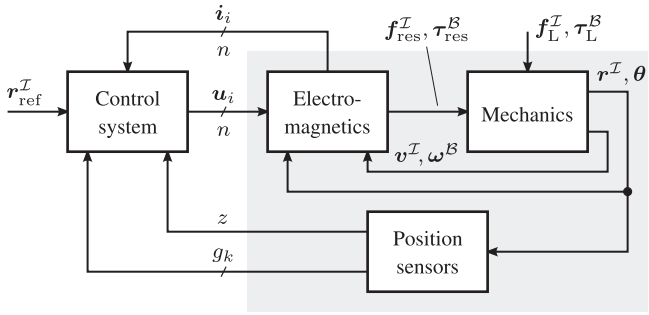


Fig. 3. Block diagram of the motor system. The gray box presents the open-loop system model. The example system has $n = 8$ three-phase motor units and 12 air-gap sensors.

An alternative to our proposed method is a three-dimensional (3-D) finite-element method (FEM) that can account for the mover tilting. A static 3-D-FEM analysis should be performed for a range of operating points—different combinations of currents, air gaps, and tilting angles—and the obtained data could be used in the form of lookup tables. However, 3-D-FEM analysis is extremely time consuming and computationally demanding. Our approach of spatial discretization resembles slice modeling that is commonly applied to the numerical modeling of 3-D effects in rotating machines [30]. Furthermore, distantly similar lumped-element modeling[1] has been used in [26] and [31]–[33]. The electromagnetic subsystem of the developed 6DOF model can be parameterized based on static 2-D FEM computations at a range of uniform air-gap and current values. Alternatively, the model could be parameterized by means of measured data. The model is validated through a comparison between the time-domain simulation results and the experimental results.

## II. Proposed System Model

Fig. 3 shows an overall block diagram of the bearingless linear motor system. The open-loop system model consists of three subsystems: mechanics, electromagnetics, and position sensors. The mechanical subsystem models a 6DOF rigid body. The electromagnetic subsystem governs the electrical dynamics and the resultant force production of all $n$ motor units $(i = 1 \ldots n)$. The position sensor subsystem maps the mechanical position to the output signals of position sensors.

[1] A lumped-element dynamic model for switched reluctance machines that uses lookup tables populated by data from 2-D FEM analysis was presented in [31]. In [32], the authors divide the bulk superconductor into a number of overlapping superconducting disks in order to model the dynamics of superconducting levitation. A hybrid analytical-FEM method, where analytical functions were fitted to the FEM data, was used in [33] to derive a lumped parameter model of an electromechanical valve.

### A. Mechanical Subsystem

*1) Reference Frames:* The mechanical subsystem, illustrated in Fig. 2, models the relative motion of the mover with respect to the rail. The *inertial reference frame* $\mathcal{I}$ is fixed to the stationary rail, and the *body reference frame* $\mathcal{B}$ is fixed to the center of mass of the mover. The position of the mover mass center is expressed using the position vector $\boldsymbol{r}^{\mathcal{I}} = [x, y, z]^{\mathrm{T}}$, where the superscript $\mathcal{I}$ indicates the inertial frame and the superscript T marks the transpose.

The orientation of the body frame $\mathcal{B}$ with respect to the inertial frame $\mathcal{I}$ is defined by three Bryan angles packed into the vector $\boldsymbol{\theta} = [\theta_1, \theta_2, \theta_3]^{\mathrm{T}}$. The Bryan angles are a set of three sequential rotations in three different frames. These rotations involve two intermediate frames to go from the inertial frame to the body frame or vice versa. We apply a 1-2-3 rotation matrix [34]

$$\boldsymbol{R}(\boldsymbol{\theta}) = \boldsymbol{R}_3(\theta_3)\boldsymbol{R}_2(\theta_2)\boldsymbol{R}_1(\theta_1) \tag{1a}$$

where

$$\boldsymbol{R}_1(\theta_1) = \begin{bmatrix} 1 & 0 & 0 \\ 0 & \cos\theta_1 & \sin\theta_1 \\ 0 & -\sin\theta_1 & \cos\theta_1 \end{bmatrix} \tag{1b}$$

$$\boldsymbol{R}_2(\theta_2) = \begin{bmatrix} \cos\theta_2 & 0 & -\sin\theta_2 \\ 0 & 1 & 0 \\ \sin\theta_2 & 0 & \cos\theta_2 \end{bmatrix} \tag{1c}$$

$$\boldsymbol{R}_3(\theta_3) = \begin{bmatrix} \cos\theta_3 & \sin\theta_3 & 0 \\ -\sin\theta_3 & \cos\theta_3 & 0 \\ 0 & 0 & 1 \end{bmatrix}. \tag{1d}$$

As an example, the position vector can be transformed from the inertial frame to the body frame according to

$$\boldsymbol{r}^{\mathcal{B}} = \boldsymbol{R}(\boldsymbol{\theta})\boldsymbol{r}^{\mathcal{I}} \tag{2}$$

and the inverse transformation is $\boldsymbol{r}^{\mathcal{I}} = \boldsymbol{R}(\boldsymbol{\theta})^{\mathrm{T}}\boldsymbol{r}^{\mathcal{B}}$.

*2) Equations of Motion:* With the rigid body assumption, the translational motion of the mover in the inertial frame is governed by [35]

$$M\frac{\mathrm{d}\boldsymbol{v}^{\mathcal{I}}}{\mathrm{d}t} = \boldsymbol{f}^{\mathcal{I}}_{\mathrm{res}} + \boldsymbol{f}^{\mathcal{I}}_{\mathrm{L}} \tag{3a}$$

$$\frac{\mathrm{d}\boldsymbol{r}^{\mathcal{I}}}{\mathrm{d}t} = \boldsymbol{v}^{\mathcal{I}} \tag{3b}$$

where $M$ is the mover mass, $\boldsymbol{f}^{\mathcal{I}}_{\mathrm{res}}$ is the resultant force vector produced by the motor units, $\boldsymbol{f}^{\mathcal{I}}_{\mathrm{L}}$ is the load force vector (including the gravity), and $\boldsymbol{v}^{\mathcal{I}}$ is the velocity vector. The angular motion of the mover around its center of mass is described by

$$\boldsymbol{I}^{\mathcal{B}}\frac{\mathrm{d}\boldsymbol{\omega}^{\mathcal{B}}}{\mathrm{d}t} = \boldsymbol{\tau}^{\mathcal{B}}_{\mathrm{res}} + \boldsymbol{\tau}^{\mathcal{B}}_{\mathrm{L}} - [\boldsymbol{\omega}^{\mathcal{B}}]_{\times}\boldsymbol{I}^{\mathcal{B}}\boldsymbol{\omega}^{\mathcal{B}} \tag{4a}$$

$$\frac{\mathrm{d}\boldsymbol{\theta}}{\mathrm{d}t} = \boldsymbol{S}(\boldsymbol{\theta})\,\boldsymbol{\omega}^{\mathcal{B}} \tag{4b}$$

where $\boldsymbol{I}^{\mathcal{B}}$ is the mover inertia matrix, $\boldsymbol{\omega}^{\mathcal{B}} = [\omega_1, \omega_2, \omega_3]^{\mathrm{T}}$ is the angular velocity vector, $\boldsymbol{\tau}^{\mathcal{B}}_{\mathrm{res}}$ is the resultant torque vector produced by the motor units, and $\boldsymbol{\tau}^{\mathcal{B}}_{\mathrm{L}}$ is the load torque vector, all expressed in the body frame. The cross-product matrix corresponding to $\boldsymbol{\omega}^{\mathcal{B}}$ is given by

$$[\boldsymbol{\omega}^{\mathcal{B}}]_{\times} = \begin{bmatrix} 0 & -\omega_3 & \omega_2 \\ \omega_3 & 0 & -\omega_1 \\ -\omega_2 & \omega_1 & 0 \end{bmatrix}. \tag{5}$$

The inverse kinematic equation (4b) presents the relation between the components of the angular velocity and the rates of change of the Bryan angles [35]. The orientation of the body frame with respect to the inertial frame, i.e., the Bryan angles, are determined by integrating (4b), where

$$\boldsymbol{S}(\boldsymbol{\theta}) = \begin{bmatrix} \cos\theta_3/\cos\theta_2 & -\sin\theta_3/\cos\theta_2 & 0 \\ \sin\theta_3 & \cos\theta_3 & 0 \\ -\cos\theta_3\tan\theta_2 & \sin\theta_3\tan\theta_2 & 1 \end{bmatrix}. \tag{6}$$

An advantage of the selected set of the 1-2-3 Bryan angles is that the matrix $\boldsymbol{S}$ reduces to the 3×3 identity matrix if the system model is linearized around the zero angles. This small-angle approximation could be useful in the local stability analysis and control design.

### B. Electromagnetic Subsystem

In order to take the tilting effects on the electromagnetic subsystem into account, each motor unit is spatially discretized into $m$ identical submotor models. Each submotor is assumed to have a uniform air gap. As shown in Fig. 2, the motor units are installed in different mechanical positions with respect to the inertial frame $\mathcal{I}$. Therefore, we apply *local 2-D reference frames* fixed to the rail of each motor unit. The coordinate axes of these local inertial frames are referred to as *thrust* and *normal*, cf., Fig. 4. To simplify notation, no separate superscript is used for the local reference frames. First, the uniform air-gap model is briefly presented [24]. Then, the spatial discretization and its underlying assumptions are described.

*1) Uniform Air-Gap Model:* The thrust speed of a motor unit is denoted by $\nu_{\mathrm{t}}$, which can be expressed in electrical rad/s, $\omega_{\mathrm{t}} = (2\pi/\tau)\nu_{\mathrm{t}}$, using the rail pole pitch $\tau$. The voltage equation for a motor unit in electrical $dq$ coordinates is [24]

$$\frac{\mathrm{d}\boldsymbol{\psi}}{\mathrm{d}t} = \boldsymbol{u} - R\boldsymbol{i} - \omega_{\mathrm{t}}\boldsymbol{J}\boldsymbol{\psi} \tag{7}$$

where $R$ is the resistance, $\boldsymbol{u} = [u_{\mathrm{d}}, u_{\mathrm{q}}]^{\mathrm{T}}$ is the voltage, $\boldsymbol{i} = [i_{\mathrm{d}}, i_{\mathrm{q}}]^{\mathrm{T}}$ is the current, $\boldsymbol{\psi} = [\psi_{\mathrm{d}}, \psi_{\mathrm{q}}]^{\mathrm{T}}$ is the flux linkage, and $\boldsymbol{J} = \left[\begin{smallmatrix} 0 & -1 \\ 1 & 0 \end{smallmatrix}\right]$ is the orthogonal rotation matrix. We omit the core losses, spatial harmonics, and end effects. Therefore, for uniform air gap $\delta$, the motor unit is characterized by the nonlinear functions[2]

$$\boldsymbol{\psi} = \boldsymbol{\psi}(\boldsymbol{i}, \delta) \qquad \boldsymbol{f} = \boldsymbol{f}(\boldsymbol{i}, \delta) \tag{8}$$

[2]The reciprocal expressions $\boldsymbol{i} = \boldsymbol{i}(\boldsymbol{\psi}, \delta)$ and $\boldsymbol{f} = \boldsymbol{f}(\boldsymbol{\psi}, \delta)$ cannot be used in the resulting spatially discretized model since the submotors are connected in series.

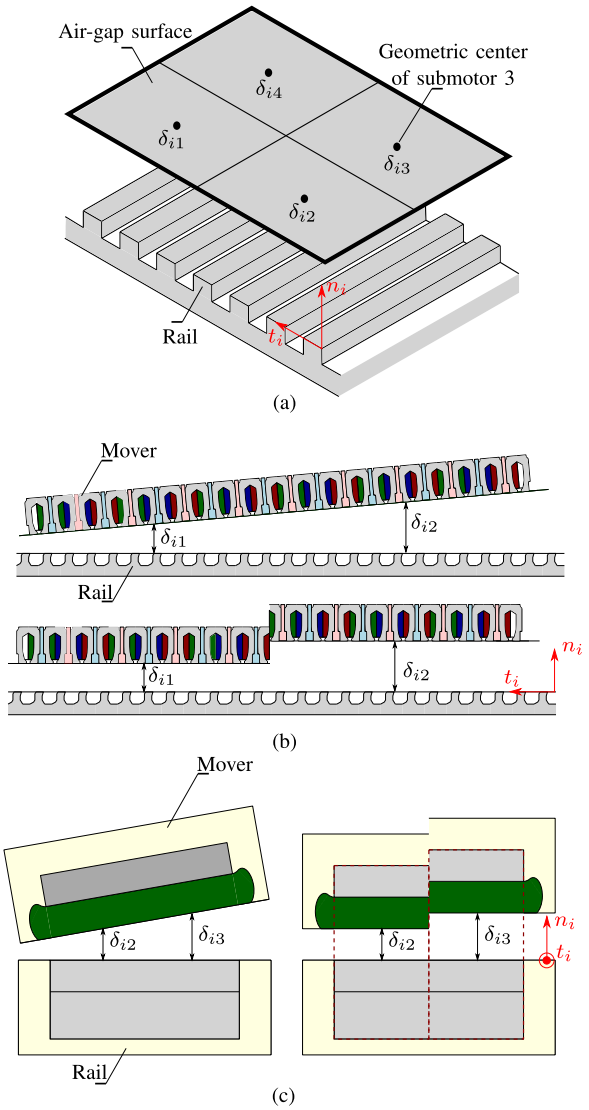


Fig. 4. Spatial discretization. (a) Single motor unit divided into four submotors. (b) Submotors along the motor length. (c) Submotors along the motor width. For each submotor, the geometric center on the air-gap surface is shown by a dot. The coordinate axes $t_i$ and $n_i$ refer to the thrust and normal directions in the local motor unit inertial frame. The uniform air gap of the $j$th submotor of the $i$th motor unit is denoted by $\delta_{ij}$.

where $\boldsymbol{f} = [f_\mathrm{t}, f_\mathrm{n}]^\mathrm{T}$ is the force vector, $f_\mathrm{t}$ is the thrust-force component, and $f_\mathrm{n}$ is the normal-force component. The functions in (8) can be computed using a static 2-D-FEM and implemented as lookup tables or explicit functions [24]. A comparatively small number of operating points is needed. Alternatively, the functions in (8) could be defined through measurements at different uniform air-gap and current values.

For the purposes of the spatial discretization, we change the independent state variable in (7) from the flux linkage to the current. Substituting the flux linkage defined in (8) into the voltage equation (7) results in

$$\boldsymbol{L}(\boldsymbol{i},\delta)\frac{\mathrm{d}\boldsymbol{i}}{\mathrm{d}t} = \boldsymbol{u} - R\boldsymbol{i} - \boldsymbol{K}(\boldsymbol{i},\delta)\boldsymbol{\nu} \tag{9}$$

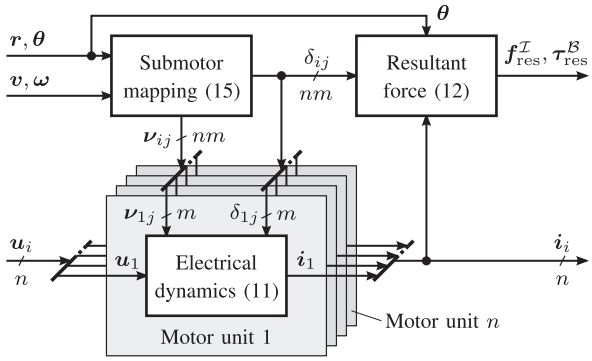


Fig. 5. Block diagram of the electromagnetic subsystem.

where the vector $\boldsymbol{\nu} = [\nu_\mathrm{t}, \nu_\mathrm{n}]^\mathrm{T}$ consists of the thrust-speed component $\nu_\mathrm{t}$ and the normal-speed component $\nu_\mathrm{n} = \mathrm{d}\delta/\mathrm{d}t$. The incremental inductance matrix and the back-EMF coefficient matrix, respectively, are given by

$$\boldsymbol{L}(\boldsymbol{i},\delta) = \frac{\partial \boldsymbol{\psi}(\boldsymbol{i},\delta)}{\partial \boldsymbol{i}} \tag{10a}$$

$$\boldsymbol{K}(\boldsymbol{i},\delta) = \left[\frac{2\pi}{\tau}\boldsymbol{J}\boldsymbol{\psi}(\boldsymbol{i},\delta) \quad \frac{\partial \boldsymbol{\psi}(\boldsymbol{i},\delta)}{\partial \delta}\right]. \tag{10b}$$

These $2 \times 2$ matrices can be computed using the known flux-linkage function $\boldsymbol{\psi}(\cdot)$ defined in (8).

*2) Spatial Discretization:* In order to model the tilting effects, each motor unit $i$ is divided into $m$ identical submotor models ($j = 1 \ldots m$) that are parameterized using the characteristics in (8). As an example, Fig. 4 illustrates the division of a motor unit into four submotors. Each submotor has its own uniform air gap $\delta_{ij}$. The submotors are assumed to be connected electrically in series. Therefore, every submotor shares the same current $\boldsymbol{i}_i$, while their flux linkages $\boldsymbol{\psi}_{ij}$ and force vectors $\boldsymbol{f}_{ij}$ are generally different due to the different air gaps. Fig. 5 shows a block diagram of the spatially discretized electromagnetic subsystem, to be described in detail in the following.

Under the aforementioned assumptions, the electrical dynamics for the $i$th motor unit in electrical $dq$ coordinates become

$$\boldsymbol{L}_i\frac{\mathrm{d}\boldsymbol{i}_i}{\mathrm{d}t} = \boldsymbol{u}_i - R\boldsymbol{i}_i - \boldsymbol{e}_i. \tag{11a}$$

The incremental inductance matrix and the induced voltage, respectively, are

$$\boldsymbol{L}_i = \frac{1}{m}\sum_{j=1}^{m}\boldsymbol{L}(\boldsymbol{i}_i,\delta_{ij}) \qquad \boldsymbol{e}_i = \frac{1}{m}\sum_{j=1}^{m}\boldsymbol{K}(\boldsymbol{i}_i,\delta_{ij})\boldsymbol{\nu}_{ij} \tag{11b}$$

where the nonlinear functions $\boldsymbol{L}(\cdot)$ and $\boldsymbol{K}(\cdot)$ are defined in (10), precomputed using the uniform air-gap 2-D-FEM data, and stored in the lookup tables.

The force vector produced by the $j$th submotor of the $i$th motor unit in its local inertial frame is $\boldsymbol{f}_{ij} = \boldsymbol{f}(\boldsymbol{i}_i,\delta_{ij})/m$, where the known force function $\boldsymbol{f}(\cdot)$, defined in (8), is used. In the global inertial frame $\mathcal{I}$, this force vector is

$$\boldsymbol{f}^{\mathcal{I}}_{ij} = \frac{1}{m}\boldsymbol{T}_i^\mathrm{T}\boldsymbol{f}(\boldsymbol{i}_i,\delta_{ij}) \tag{12a}$$

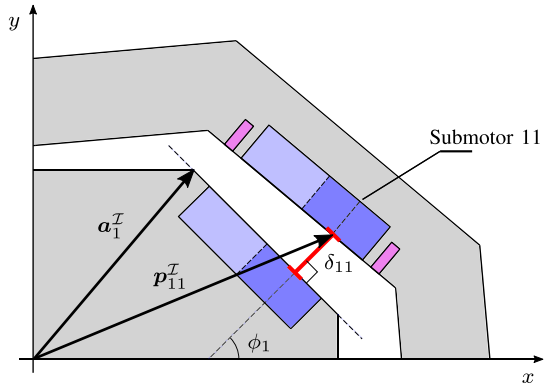


Fig. 6. Top view of the motor system showing motor unit 1. The definition of the air gap for submotor 11 is shown. The constant vector $\boldsymbol{a}_1^{\mathcal{I}}$ can be chosen arbitrarily from the rail surface (e.g., a corner or middle point).

where $\boldsymbol{T}_i$ is a constant $2 \times 3$ transformation matrix that depends on the geometrical location of the $i$th motor unit with respect to the reference frame $\mathcal{I}$. Therefore, the resultant force and associated torque vectors are

$$\boldsymbol{f}_{\text{res}}^{\mathcal{I}} = \sum_{i=1}^{n}\sum_{j=1}^{m} \boldsymbol{f}_{ij}^{\mathcal{I}} \tag{12b}$$

$$\boldsymbol{\tau}_{\text{res}}^{\mathcal{B}} = \sum_{i=1}^{n}\sum_{j=1}^{m} [\boldsymbol{l}_{ij}^{\mathcal{B}}]_{\times} \boldsymbol{R}(\boldsymbol{\theta}) \boldsymbol{f}_{ij}^{\mathcal{I}} \tag{12c}$$

where $\boldsymbol{l}_{ij}^{\mathcal{B}}$ is the lever arm vector of the $ij$th submotor. This vector is constant for each submotor and is defined from the mover's center of mass to the geometric center of the air-gap surface [cf. Fig. 4(a)] of that submotor. The cross-product matrices are formed as in (5). For the geometry under consideration, the transformation matrix $\boldsymbol{T}_i$ needed in (12a) is

$$\boldsymbol{T}_i = \begin{bmatrix} 0 & 0 & 1 \\ \cos\phi_i & \sin\phi_i & 0 \end{bmatrix} \tag{13}$$

where $\phi_i$ is a constant angle. Fig. 6 defines the angle $\phi_1$ for motor unit 1. The angles of other motor units are obtained similarly.

*3) Submotor Mapping:* The electrical dynamics (11) and force production (12) require the air-gap value $\delta_{ij}$ and the velocity vector $\boldsymbol{\nu}_{ij}$ of each submotor. As previously mentioned, the lever-arm vector $\boldsymbol{l}_{ij}^{\mathcal{B}}$ is constant and known in the body frame. The position of the geometrical center of the $ij$th submotor air-gap surface in the inertial frame is

$$\boldsymbol{p}_{ij}^{\mathcal{I}} = \boldsymbol{r}^{\mathcal{I}} + \boldsymbol{R}(\boldsymbol{\theta})^{\mathrm{T}} \boldsymbol{l}_{ij}^{\mathcal{B}}. \tag{14}$$

As shown in Fig. 6, the air gap of each submotor is calculated as the shortest distance from the geometrical center of the submotor air-gap surface to the rail surface, i.e.,

$$\delta_{ij} = \begin{bmatrix} 1 & 0 & 0 \end{bmatrix} \boldsymbol{R}_3(\phi_i) \left(\boldsymbol{p}_{ij}^{\mathcal{I}} - \boldsymbol{a}_i^{\mathcal{I}}\right) \tag{15a}$$

where the constant vector $\boldsymbol{a}_i^{\mathcal{I}}$ defines an arbitrary point at the rail surface, $\boldsymbol{R}_3$ given in (1d) is the rotation matrix about the $z$-axis, and the constant angle $\phi_i$ depends on the geometry according to Fig. 6. Furthermore, the position $\boldsymbol{p}_{ij}^{\mathcal{I}}$ can also be expressed in the local motor unit frame as $\boldsymbol{p}_{ij} = \boldsymbol{T}_i \boldsymbol{p}_{ij}^{\mathcal{I}}$, where the $2\times3$ constant transformation matrix $\boldsymbol{T}_i$ is given in (13). Therefore, the submotor velocity vector consisting of the thrust-speed and normal-speed components is

$$\boldsymbol{\nu}_{ij} = \frac{\mathrm{d}\boldsymbol{p}_{ij}}{\mathrm{d}t} = \boldsymbol{T}_i \left(\boldsymbol{v}^{\mathcal{I}} + [\boldsymbol{\omega}^{\mathcal{B}}]_{\times} \boldsymbol{l}_{ij}^{\mathcal{B}}\right). \tag{15b}$$

As a result, the submotor mapping block in Fig. 5 provides the air-gap value and the velocity vector of each submotor based on the mechanical states $\boldsymbol{r}$, $\boldsymbol{\theta}$, $\boldsymbol{v}$, and $\boldsymbol{\omega}$.

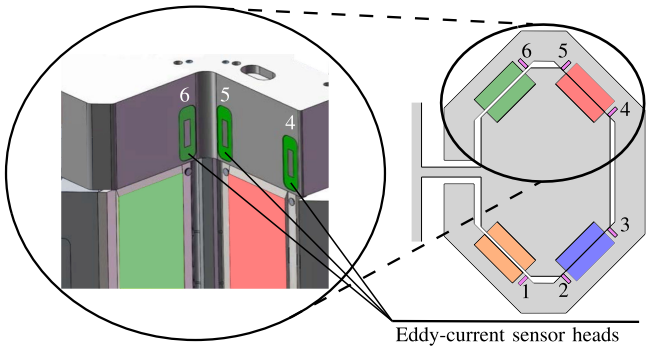


Fig. 7. Sensor housing assembly and the positions of the eddy-current sensor heads.

### C. Position Sensors

The example motor system has 12 eddy-current air-gap sensors: six sensors are located in the upper section [cf. Fig. 2(a)] and the other six are located in the lower section of the mover. As shown in Fig. 7, the sensors are placed in a sensor housing assembly that is attached to the uppermost and similarly to the lowermost parts of the mover. Furthermore, the $z$-axis position is measured with a separate laser sensor. These sensor outputs have to be included in the system model in order to be able to close the control loops. The constant vector $\boldsymbol{\ell}_k^{\mathcal{B}}$ defines the coordinates of the $k$th sensor in the body frame. Hence, the air-gap sensor location in the inertial frame is

$$\boldsymbol{s}_k^{\mathcal{I}} = \boldsymbol{r}^{\mathcal{I}} + \boldsymbol{R}(\boldsymbol{\theta})^{\mathrm{T}} \boldsymbol{\ell}_k^{\mathcal{B}}. \tag{16}$$

Similarly to (15a), the output of the air-gap sensors is assumed to be the shortest distance from the sensor to the corresponding rail surface, i.e.,

$$g_k = \begin{bmatrix} 1 & 0 & 0 \end{bmatrix} \boldsymbol{R}_3(\phi_k) \left(\boldsymbol{s}_k^{\mathcal{I}} - \boldsymbol{b}_k^{\mathcal{I}}\right) \tag{17}$$

where the constant vector $\boldsymbol{b}_k^{\mathcal{I}}$ defines an arbitrary point at the rail-side surface corresponding to the $k$th sensor. In addition, the $z$-axis position can be easily obtained from the position vector $\boldsymbol{r}^{\mathcal{I}}$. Naturally, the position sensor models could be augmented with models for the measurement noise and sensor nonlinearities.

## III. Experimental Setup and Control System

### A. Experimental Setup

Fig. 8 shows a photograph of the experimental 6DOF bearingless linear motor system. The mover mass is $M = 150$ kg and

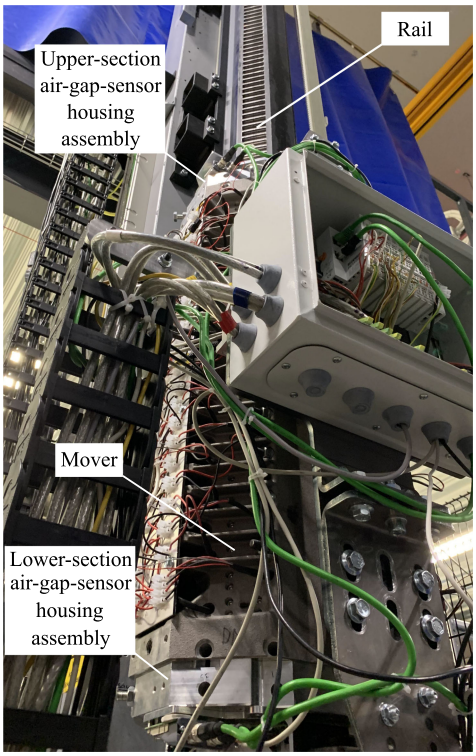


Fig. 8. Photograph of the experimental setup, showing the mover, the vertical rail, and the air-gap sensor assemblies in the upper and lower sections.

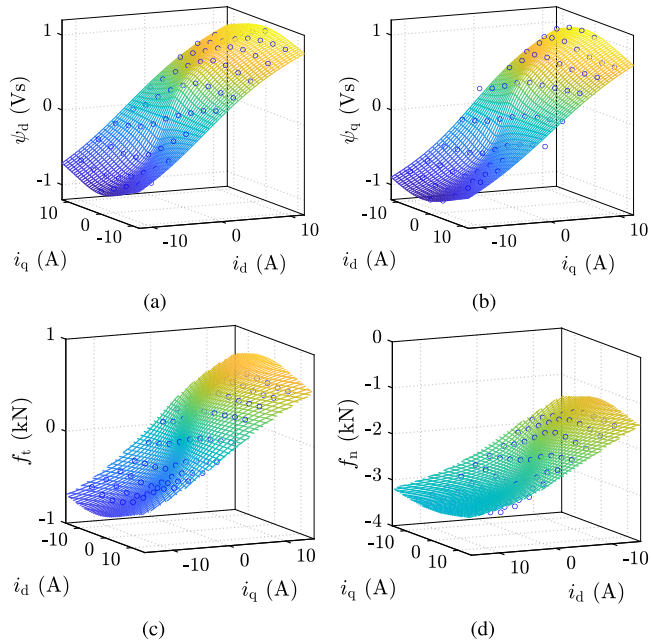


Fig. 9. Flux linkages and forces as function of currents at constant air gap $\delta = 1.25$ mm. (a) $\psi_d$. (b) $\psi_q$. (c) $f_t$. (d) $f_n$. The blue circles present the FEM data. The surfaces correspond to the fitted magnetic model [24].

the mover inertia matrix is $\boldsymbol{I}^{\mathcal{B}} = \mathrm{diag}(10.2, 10.9, 5.0)$ kg·m$^2$. The motor system consists of eight 2-kW three-phase linear FSPM motor units. Each of these motor units is fed by an individual inverter with a 540-V dc-bus voltage. The continuous rated current of the motor units is 10 A (rms) and the rated speed is 1 m/s. When the mover is at the center position, the electromagnetic air gap of the motor units is $\delta = 1.05$ mm. As an example, Fig. 9 presents the electromagnetic characteristics (8) of the motor units at $\delta = 1.25$ mm.[3] These characteristics were computed with the 2-D-FEM, where the materials were assumed to be homogeneous and isotropic. Furthermore, the end effects and eddy currents were neglected.

### B. Control System

Fig. 10 shows a simplified block diagram of the 6DOF control system, based on the 2DOF control scheme presented in [23]. This 6DOF control system is a preliminary version to be improved in the future, and we do not consider it as a contribution of this work. However, due to the unstable nature of the open-loop system, some control system is necessary for performing simulations and experiments.

The current controllers form the inner control loop, and the levitation and traction controllers form the outer loop. The input signals for each current controller are the reference current $\boldsymbol{i}_i^{\mathrm{ref}}$,

[3]The FEM data were computed at the air-gap values {0.05, 0.45, 0.85, 1.25, 1.65, 2.05, 2.45} mm, where 1.25 mm is the original nominal air gap of the motor unit. When the mover of the experimental setup is at its center position, the air gap is slightly less (1.05 mm) due to manufacturing tolerances.

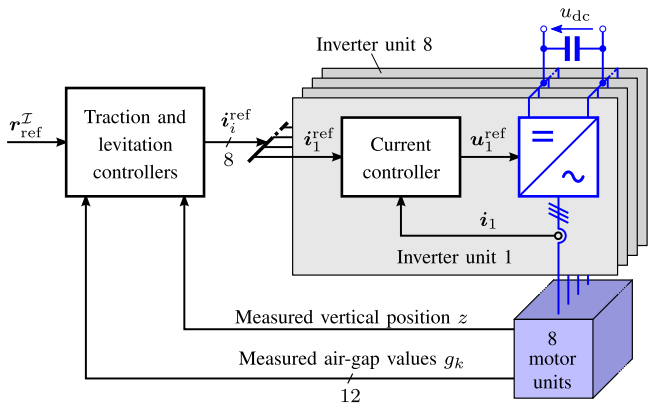


Fig. 10. Block diagram of the control system for the motor system. Each motor unit is controlled by its own inverter. The traction and levitation controllers block consists of four differential air-gap controllers, a rotation, and a traction controller.

the measured current $\boldsymbol{i}_i$, the dc-link voltage $u_{\mathrm{dc}}$, and the vertical position $z$ (for the $dq$ transformation). Each voltage reference $\boldsymbol{u}_i^{\mathrm{ref}}$ is fed to the pulsewidth modulator.

The levitation controller consists of four decentralized differential air-gap controllers and a rotation controller. The differential air gaps are

$$d_1 = (g_1 - g_5)/2 \qquad d_2 = (g_6 - g_2)/2$$
$$d_3 = (g_7 - g_{11})/2 \qquad d_4 = (g_8 - g_{12})/2 \tag{18}$$

where $g_1 \ldots g_{12}$ are the measured air-gap values, cf. Fig. 11. Opposing motor units (i.e., units 1 and 3, units 2 and 4, etc.) form pairs. The references for the differential air gaps are set to zero. Each differential air-gap controller adjusts the normal

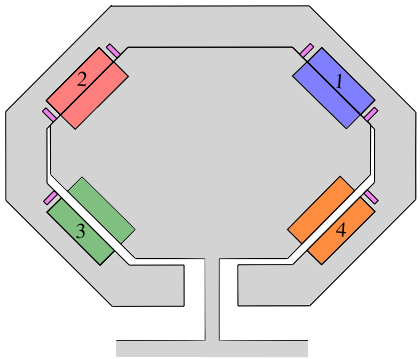


Fig. 11. Initial configuration of the mover for performing the simulations and experimental tests. The air gaps of motor units 1 and 2 are zero, while motor units 3 and 4 have the maximum air gap.

forces of its opposing motor units in order to drive the measured differential air gap to zero [23].

The rotation controller regulates the angle $\theta_3$ defined in Fig. 2(a). This angle is estimated using the measured air-gap values

$$\theta_3 = \frac{1}{4}\left[\arcsin\left(\frac{g_2 - g_3}{c}\right) + \arcsin\left(\frac{g_4 - g_5}{c}\right) + \arcsin\left(\frac{g_8 - g_9}{c}\right) + \arcsin\left(\frac{g_{10} - g_{11}}{c}\right)\right] \quad (19)$$

where $c$ is the distance between the sensor pairs (i.e., sensors 2 and 3, sensors 4 and 5, etc.).

In (19), the average of the estimated angles from all the four sensor pairs provides a more accurate angle estimate as compared to the angle estimated using only one sensor pair. The rotation controller adjusts the normal forces of all the motor units simultaneously according to their force lever in order to drive $\theta_3$ to zero. The two remaining rotation angles are stabilized indirectly via the differential air-gap controllers. These angles are a result of different differential air gaps in the upper and lower section. Thus, driving the differential air gaps of all the motor pairs to zero stabilizes these small angles.

The traction controller drives the mover along the rail according to the reference position. This controller additionally counteracts the gravity. The reference thrust force is divided equally between the motor units, i.e., each motor unit contributes 1/8 of the total required thrust force.

The controllers have been tuned based on the desired bandwidth of their corresponding control loop [23]. The closed-loop bandwidth of the current controllers are 700 Hz, and the bandwidth of the speed control loop and position control loop of the differential air-gap controllers are 30 and 3 Hz, respectively. Furthermore, a separate full-order state observer provides the speed and position estimates for each differential air-gap controller.

## IV. Results

In this section, the developed model is evaluated by comparing the time-domain simulation results and the experimental results. The same control system is used for both simulations and experiments. However, due to the discrepancies between the FEM data and the real characteristics of the motor units, the controllers have been parameterized differently in the simulations and the experiments in order to achieve approximately equal closed-loop bandwidths.

The FEM results match very well with the characteristics of the actual motor units around the nominal air gap. However, at small air-gap values, there are significant discrepancies between the FEM data and the measured data. These differences are attributed to the manufacturing tolerances, i.e., the dimensions used in the FEM model slightly differ from those of the actual prototype. Furthermore, as the air gap approaches zero, the magnetic circuit becomes essentially short-circuited, which increases the sensitivity of the FEM model to the BH curve. The real BH curve is not perfectly known at very high flux densities. Moreover, the air-gap mesh density in the FEM affects the accuracy, particularly at very small air-gap values [36]. As a result, the FEM analysis only provides an approximation of the actual characteristics. This issue could be tackled by characterizing the motor units experimentally.

### A. Time-Domain Simulations

The model shown in Fig. 3 was implemented in the MATLAB/Simulink environment. The nonlinear functions in (8) were implemented as lookup tables, whose data are obtained from static 2-D-FEM analysis. Additionally, the partial derivatives in (10) were precomputed using the same 2-D-FEM data and implemented as lookup tables.

In the first simulation, the initial position of the mover is chosen as in Fig. 11. In this position, motor units 1 and 2 in the upper section as well as motor units 5 and 6 in the lower section of the mover are attached to the rail. The four remaining motor units in the lower and upper sections are fully detached. Fig. 12(a) shows the simulation results corresponding to this initial position. The differential air-gap controllers are enabled at $t = 0.4$ s, while the rotation controller is intentionally disabled. This test demonstrates the effect of the unbalanced magnetic torque when active rotation control is disabled. As a result, the levitation controllers attempt to minimize the differential air gaps via changes in the currents. At about $t = 0.55$ s, the differential air gaps are almost zero, but due to the unbalanced magnetic torque, the mover begins to rotate until it reaches its physical rotation limit. It can be seen that the unstable (or marginally stable) mode related to the rotation is initially slow under the ideal operating conditions. If measurement noise or some other disturbances were added to the simulation model, the rotation would happen faster.

At $t = 0.65$ s, the changes in the differential air gaps due to the rotation lead to slight adjustments in the currents by the differential air-gap controllers. At this point, since $\theta_3$ is at its maximum, and the mover is completely rotated in a clockwise direction, the differential air gaps $d_1$ and $d_2$ are zero. Thus, there is no error between the reference differential air gaps and their actual values. In this operating point, the currents are close to zero, as seen in Fig. 12(a).

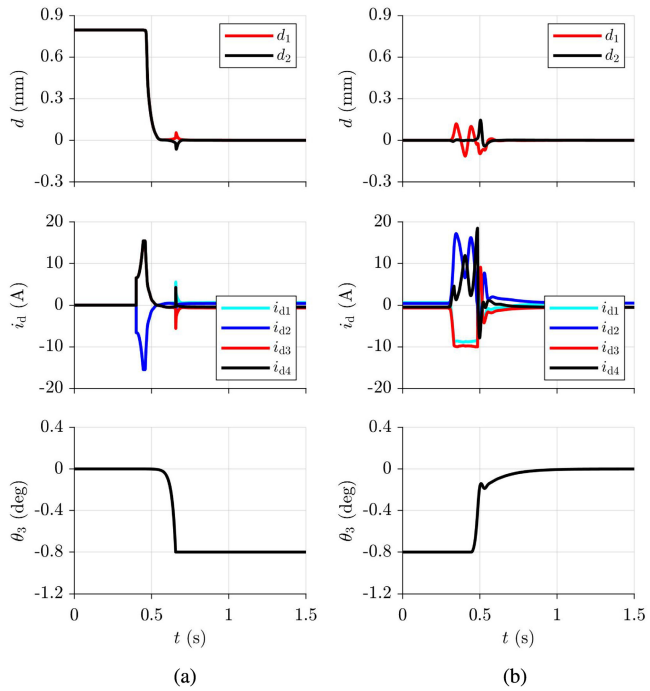


Fig. 12. Simulation results showing the differential air gaps and the currents of the upper section motor units, and rotation angle $\theta_3$. (a) Air-gap controllers are enabled at $t = 0.4$ s, while the rotation controller is disabled. (b) Mover is rotated and the air-gap controllers are already enabled, but the rotation controller is enabled at $t = 0.3$ s.

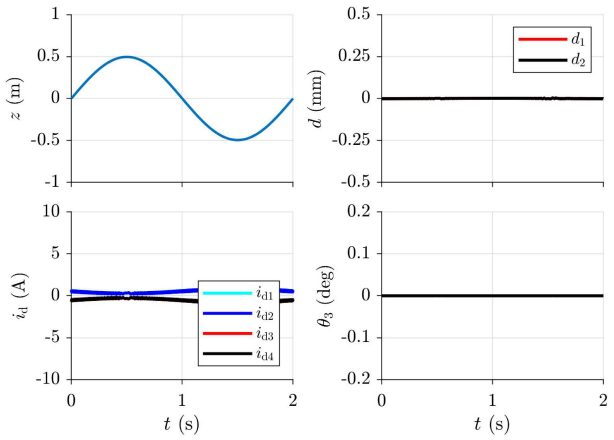


Fig. 13. Simulation results with a sinusoidal $z$-axis position reference. The subplots show the $z$-axis position, differential air gap, $d$-axis currents, and rotation angle $\theta_3$.

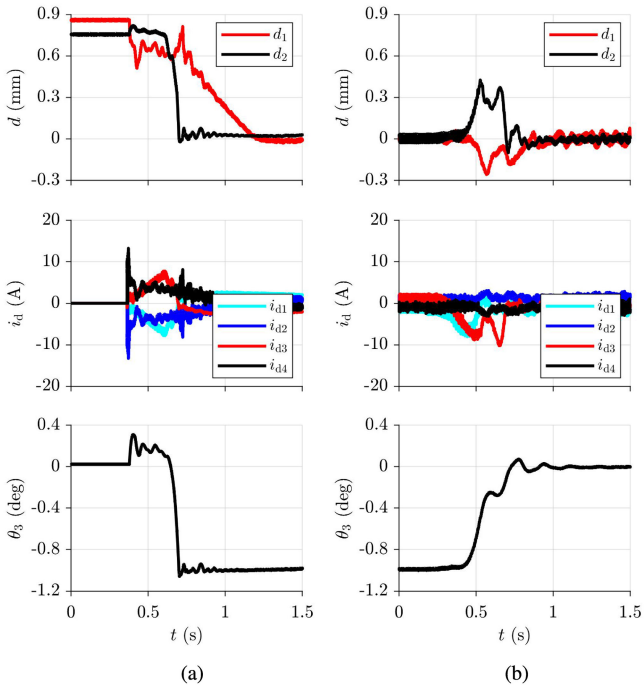


Fig. 14. Experimental results showing the differential air gaps and the currents of the upper section motor units, and the rotation angle $\theta_3$. (a) Air-gap controllers are enabled at $t = 0.4$ s, while the rotation controller is disabled. (b) Mover is rotated and the air-gap controllers are already enabled, but the rotation controller is enabled at $t = 0.3$ s.

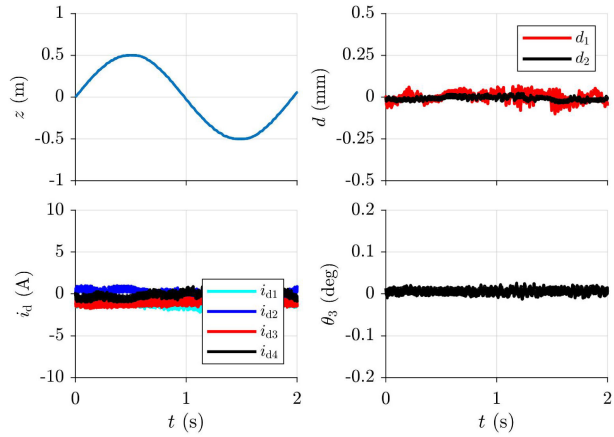


Fig. 15. Experimental results with a sinusoidal $z$-axis position reference. The subplots show the $z$-axis position, differential air gap, $d$-axis currents, and rotation angle $\theta_3$.

In the second simulation, cf. Fig. 12(b), the mover is at its maximum rotational angle $\theta_3$ and the differential air-gap controllers are active. The rotation controller is enabled at $t = 0.3$ s. Thus, this controller regulates the motor unit currents in order to rotate the mover counterclockwise and to force this rotation angle to zero. After some transients, the rotation angle reaches zero at about $t = 1$ s.

Fig. 13 shows the last simulation result where the system tracks a sinusoidal vertical ($z$-axis) reference. The system is already levitated, and all the differential air-gap and rotation controllers are active. As the system follows the reference signal, the other controllers maintain the levitation.

### B. *Experimental Results*

Figs. 14 and 15 show the experimental results corresponding to the simulation cases. Clearly, there are differences between the simulation and measurement results, but the overall behavior of the simulation model is relatively similar to that of the actual

system. The other differences originate partly from the manufacturing tolerances in the mechanical structure of the prototype system and the eddy-current air-gap sensors. Furthermore, as already mentioned, the magnetic characteristics of the motor units differ significantly from the FEM data at small air-gap values, which particularly affects the modeling accuracy in the tests shown in Fig. 14. It can also be seen in Fig. 14(a) that the rotation of the mover happens earlier than in the corresponding simulation. This difference is due to noise and other nonidealities that drive the system faster away from the marginally stable operating point.

## V. Conclusion

In this article, a dynamic lumped-element model for a 6DOF bearingless linear motor was derived. The model includes three subsystems: mechanical, electromagnetic, and position sensors. The mechanical subsystem models a 6DOF rigid-body mover. The electromagnetic subsystem incorporates the electrical dynamics together with the force production. The effect of the tilting of the mover on the electromagnetic force and its associated torque production was taken into account by using a lumped-element modeling approach. Dividing the armature into several submotors—each having a different uniform air gap in a tilted position—enabled us to integrate the tilting effects into the model.

A four-sided bearingless linear FSPM motor system was applied in the example system. The developed model was tested by comparing the time-domain simulation results to the experimental results obtained using a prototype motor system. This comparison showed differences that are attributable to the manufacturing tolerances and the inaccuracies of the FEM data at very small air-gap values. Nevertheless, a relatively similar overall behavior was observed.

The developed model can be used in stability analysis, time-domain simulations, and control design of 6DOF bearingless linear motor systems. Future research could be conducted to characterize the motor units experimentally in order to replace the FEM-based characteristics with the measured characteristics in the lookup tables of the model. Although linear FSPM motor units and the four-sided configuration were considered in this work, the modeling concept can be applied to other motor types and other configurations as well.

## Acknowledgment

The authors would like to thank Dr. S. E. Saarakkala for his contributions on the development of the control system. The authors would also like to thank T. Hakala, P. Raassina, T. Korhonen, S. Suur-Askola, and T. Purosto for insightful comments and help with the experimental setup.

## References

[1] J. F. Gieras, Z. J. Piech, and B. Tomczuk, *Linear Synchronous Motors: Transportation and Automation Systems*, *2nd ed.* Boca Raton, FL, USA: CRC Press, 2012.

[2] I. Boldea, L. N. Tutelea, W. Xu, and M. Pucci, "Linear electric machines, drives, and MAGLEVs: An overview," *IEEE Trans. Ind. Electron.*, vol. 65, no. 9, pp. 7504–7515, Sep. 2018.

[3] K. Yoshida and H. Matsumoto, "Propulsion and guidance simulation of a high-temperature superconducting bulk ropeless linear elevator," *IEEE Trans. Magn.*, vol. 40, no. 2, pp. 615–618, Mar. 2004.

[4] K. Yoshida and X. Zhang, "Propulsion and guidance control in ropeless linear elevator with pitching motion," in *Proc. Int. Conf. Elect. Mach. Syst.*, Nanjing, China, Sep. 2005, vol. 3, pp. 1887–1892.

[5] B. Schmulling, O. Effing, and K. Hameyer, "State control of an electromagnetic guiding system for ropeless elevators," in *Proc. Eur. Conf. Power Electron. Appl.*, Aalborg, Denmark, Sep. 2007, pp. 1–10.

[6] H. S. Lim and R. Krishnan, "Ropeless elevator with linear switched reluctance motor drive actuation systems," *IEEE Trans. Ind. Electron.*, vol. 54, no. 4, pp. 2209–2218, Aug. 2007.

[7] A. Onat, E. Kazan, N. Takahashi, D. Miyagi, Y. Komatsu, and S. Markon, "Design and implementation of a linear motor for multicar elevators," *IEEE/ASME Trans. Mechatronics*, vol. 15, no. 5, pp. 685–693, Oct. 2010.

[8] S. Lee, S. Kim, S. Saha, Y. Zhu, and Y. Cho, "Optimal structure design for minimizing detent force of PMLSM for a ropeless elevator," *IEEE Trans. Magn.*, vol. 50, no. 1, pp. 1–4, Jan. 2014.

[9] H. Fan, K. T. Chau, C. Liu, L. Cao, and T. W. Ching, "Quantitative comparison of novel dual-PM linear motors for ropeless elevator system," *IEEE Trans. Magn.*, vol. 54, no. 11, pp. 1–6, Nov. 2018.

[10] B. Zhang, M. Cheng, S. Zhu, M. Zhang, W. Hua, and R. Cao, "Investigation of linear flux-switching permanent magnet machine for ropeless elevator," in *Proc. Int. Conf. Elect. Mach. Syst.*, Chiba, Japan, Nov. 2016, pp. 1–5.

[11] I. Petrov, T. Purosto, T. Hakala, and J. Ratia, "Electric linear motor," U. S. Patent 10 858 219 (B2), Dec. 8, 2020.

[12] T. Korhonen *et al.*, "Electric linear motor," *U. S. Patent* 10 689 227 (B2), Jun. 23, 2020.

[13] E. Hoang, A. H. Ben-Ahmed, and J. Lucidarme, "Switching flux permanent magnet polyphased synchronous machines," in *Proc. Eur. Conf. Power Electron. Appl.*, Trondheim, Norway, Sep. 1997, vol. 3, pp. 903–908.

[14] C. F. Wang, J. X. Shen, L. L. Wang, and K. Wang, "A novel permanent magnet flux-switching linear motor," in *Proc. IET Conf. Power Electron., Mach. Drives*, York, U.K., Apr. 2008, pp. 116–119.

[15] Z. Q. Zhu, X. Chen, J. T. Chen, D. Howe, and J. S. Dai, "Novel linear flux-switching permanent magnet machines," in *Proc. Int. Conf. Elect. Mach. Syst.*, Wuhan, China, Oct. 2008, pp. 2948–2953.

[16] M.-J. Jin, C.-F. Wang, J.-X. Shen, and B. Xia, "A modular permanent-magnet flux-switching linear machine with fault-tolerant capability," *IEEE Trans. Magn.*, vol. 45, no. 8, pp. 3179–3186, Aug. 2009.

[17] L. Huang, H. Yu, M. Hu, J. Zhao, and Z. Cheng, "A novel flux-switching permanent-magnet linear generator for wave energy extraction application," *IEEE Trans. Magn.*, vol. 47, no. 5, pp. 1034–1037, May 2011.

[18] R. Cao, M. Cheng, C. Mi, W. Hua, X. Wang, and W. Zhao, "Modeling of a complementary and modular linear flux-switching permanent magnet motor for urban rail transit applications," *IEEE Trans. Energy Convers.*, vol. 27, no. 2, pp. 489–497, Jun. 2012.

[19] L. Huang, H. Yu, M. Hu, and H. Liu, "Study on a long primary flux-switching permanent magnet linear motor for electromagnetic launch systems," *IEEE Trans. Plasma Sci.*, vol. 41, no. 5, pp. 1138–1144, May 2013.

[20] Y. Amara, G. Barakat, J. Paulides, and E. Lomonova, "Overload capability of linear flux switching permanent magnet machines," *Appl. Mech. Mater.*, vol. 416–417, pp. 345–352, Sep. 2013.

[21] A. Chiba, T. Fukao, O. Ichikawa, M. Oshima, M. Takemoto, and D. G. Dorrell, *Magnetic Bearings and Bearingless Drives*, *1st ed.* Burlington, MA, USA: Newnes, 2005.

[22] R. P. Jastrzebski, P. Jaatinen, and O. Pyrhönen, "Modeling and control design simulations of a linear flux-switching permanent-magnet-levitated motor," *Mech. Eng. J.*, vol. 4, no. 5, pp. 1–12, Jul. 2017.

[23] S. E. Saarakkala, M. Sokolov, R. Hosseinzadeh, and M. Hinkkanen, "Levitation control for a double-sided bearingless linear motor based on feedback linearization," in *Proc. IEEE Energy Convers. Congr. Expo.*, Baltimore, MD, USA, Sep./Oct. 2019, pp. 4923–4930.

[24] M. Sokolov, S. E. Saarakkala, R. Hosseinzadeh, and M. Hinkkanen, "A dynamic model for bearingless flux-switching permanent-magnet linear machines," *IEEE Trans. Energy Convers.*, vol. 35, no. 3, pp. 1218–1227, Sep. 2020.

[25] S. MiriĆ, P. Küttel, A. TüysüzJ. W. Kolar, "Design and experimental analysis of a new magnetically levitated tubular linear actuator," *IEEE Trans. Ind. Electron.*, vol. 66, no. 6, pp. 4816–4825, Jun. 2019.

[26] S. Mirić, R. Giuffrida, D. Bortis, and J. Kolar, "Dynamic electromechanical model and position controller design of a new high-precision self-bearing linear actuator," *IEEE Trans. Ind. Electron.*, vol. 68, no. 1, pp. 744–755, Jan. 2021.

[27] F. Poltschak, "Bearing-less four-coil oscillatory linear motor," in *Proc. Linear Drives Ind. Appl.*, Neuchâtel, Switzerland, Jul. 2019, pp. 1–5.
[28] N. Tsai and C. Chiang, "High-frequency linear compressor and lateral position regulation," *IEEE Trans. Control Syst. Technol.*, vol. 20, no. 1, pp. 127–138, Jan. 2012.
[29] J. de Boeij, E. Lomonova, and J. Duarte, "Contactless planar actuator with manipulator: A motion system without cables and physical contact between the mover and the fixed world," *IEEE Trans. Ind. Appl.*, vol. 45, no. 6, pp. 1930–1938, Nov./Dec. 2009.
[30] J. J. C. Gyselinck, L. Vandevelde, and J. A. A. Melkebeek, "Multi-slice FE modeling of electrical machines with skewed slots-the skew discretization error," *IEEE Trans. Magn.*, vol. 37, no. 5, pp. 3233–3237, Sep. 2001.
[31] T. C. O'Connell, J. R. Wells, and O. A. Watts, "A lumped-parameter off-axis-capable dynamic switched reluctance machine model including unbalanced radial forces," *IEEE Trans. Energy Convers.*, vol. 30, no. 1, pp. 161–174, Mar. 2015.
[32] C. S. Hearn, S. B. Pratap, D. Chen, and R. G. Longoria, "Dynamic performance of lumped parameter model for superconducting levitation," *IEEE Trans. Appl. Supercond.*, vol. 26, no. 6, pp. 1–8, Sep. 2016.
[33] A. di Gaeta, L. Glielmo, V. Giglio, and G. Police, "Modeling of an electromechanical engine valve actuator based on a hybrid analytical- FEM approach," *IEEE/ASME Trans. Mechatronics*,, vol. 13, no. 6, pp. 625–637, Dec. 2008.
[34] J. Wittenburg, *Dynamics of Multibody Systems*, *2nd ed.*Berlin, Germany: Springer, 2008.
[35] N. J. Kasdin and D. A. Paley, *Engineering Dynamics: A Comprehensive Introduction*. Princeton, NJ, USA: Princeton Univ. Press, 2011.
[36] K. Adamiak, J. Mizia, G. E. Dawson, and A. R. Eastham, "Finite element force calculation in linear induction machines," *IEEE Trans. Magn.*, vol. 23, no. 5, pp. 3005–3007, Sep. 1987.

**Reza Hosseinzadeh** received the B.Sc.(Eng.) degree in electrical engineering from the Islamic Azad University, Bushehr, Iran, in 2009, and the M.Sc.(Tech.) degree in electrical engineering from the Aalto University, Espoo, Finland, in 2019, where he is currently working toward the D.Sc.(Tech.) degree.

His main research interests include bearingless motors, electric drives, and control systems.

**Floran Martin** received the Engineering Diploma in electrical engineering from Polytech Nantes, Nantes, France, in 2009, and the M.S. and Ph.D. degrees in electrical engineering from the University of Nantes, Nantes, in 2009 and 2013, respectively.

In 2014, he joined the Department of Electrical Engineering and Automation, Aalto University, Espoo, Finland, where he is currently a Staff Scientist. His research interests include modeling of magnetic materials as well as analyzing, designing, and controlling electrical machines.

**Marko Hinkkanen** (Senior Member, IEEE) received the M.Sc. (Eng.) and D.Sc.(Tech.) degrees in electrical engineering from the Helsinki University of Technology, Espoo, Finland, in 2000 and 2004, respectively.

He is currently an Associate Professor with the School of Electrical Engineering, Aalto University, Espoo. His research interests include control systems, electric drives, and power converters.

Dr. Hinkkanen was a General Co-Chair for the 2018 IEEE 9th International Symposium on Sensorless Control for Electrical Drives. He was the corecipient of the 2016 International Conference on Electrical Machines Brian J. Chalmers Best Paper Award, the 2016 and 2018 IEEE Industry Applications Society Industrial Drives Committee Best Paper Awards, and the 2020 SEMIKRON Innovation Award. He is an Associate Editor for the IEEE TRANSACTIONS ON ENERGY CONVERSION and the *IET Electric Power Applications*.